LANGMUIR

pubs.acs.org/Langmuir Article

An Ultralight Capillary-Driven Heat Pipe

Yong Ju Lee, Yi Xiang Wang, Yoon Chang Jeong, Michael D. Atkins, Kiju Kang,* and Tongbeum Kim

Cite This: *Langmuir* 2024, 40, 8194–8204 Read Online

ABSTRACT: Capillary-driven heat pipes are an effective thermal solution for compacting electronic cooling systems. We advance such a heat pipe thermal solution with ultralightweighting for mobile applications. In our advancement, the envelope that encapsulates the phase-change process of a working fluid is fabricated via electroless plating being ∼40 μm thick. Furthermore, the wick structure that transports condensate to a heat source via capillarity is also electroless-plated onto the envelope's inner surfaces, creating a 100-μm-thick, microporous layer. This wick structure is sequentially superhydrophilized by blackening that forms a nanotexture on the microporous wick layer. An effective density of our prototype ultralight heat pipes (uHPs), as a measure of lightweighting, indicates, on average, a remarkable 73% weight reduction of commercial counterparts with sintered copper powder wick in similar exterior dimensions (e.g., ∼2.7 g, compared to ∼10.0 g) while providing equivalent heat spreading. Furthermore, the uHP operates at a 25% lower evaporator temperature, due to additional heat rejection to the surroundings through the ultrathin-walled envelope and wick.

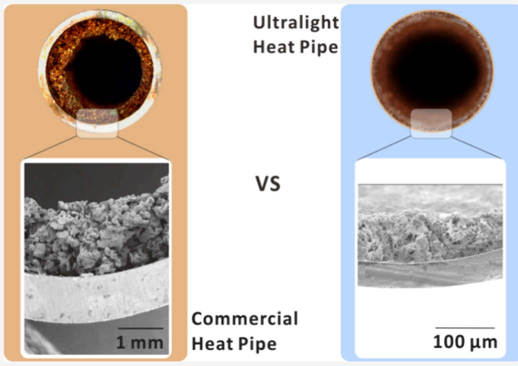

■ INTRODUCTION

A capillary-driven heat pipe is perhaps the most popular contemporary solution for thermally managing microelectronic components, due to its simple design, low cost, design flexibility, and good heat spreading capability.[1−3] A notable application includes smartphones and notebook computers after flattening the generic tubular design for the sake of further compacting. A heat pipe, in principle, spreads excessive heat emitted from microelectronic components via latent heat conversion of a working fluid in a vacuum chamber (often termed an "envelope"). Both hot and cold ends of the envelope act as an evaporator and a condenser, respectively, while the midsection functions to provide passages for (i) vapor flow (from the hot end to the cold end) via a central hollow region and (ii) condensate flow (from the cold end to the hot end) through the wick structure by capillarity. In the midsection, both vapor and condensate flow counter-currently, separated by the free surface interface caused by surface-tension fluid forces. The design objective of a heat pipe is to lower the operating temperature of the component attached to the evaporator end by permitting the transportation of heat along the heat pipe and heat rejection at the condenser end.

The overall heat spreading of a generic tubular capillary-driven heat pipe (Figure 1) is strongly dependent on the design of the wick structure. Thus far, various wicking media have been developed and commercialized. They include sintered powders,[4] grooves,[5] and screen meshes.[6] Among these wick structures, copper powders that are sintered onto the inner surface of a tubular copper envelope are predominant (Figure 1). This is largely due to the following advantages: (i) high thermal conductivity and low thermal resistance that allow for good heat transfer between both hot and cold ends,[7] (ii) high capillary pressure that can overcome the viscous and gravitational forces that opposes the condensate flow in the wick,[8] (iii) good mechanical strength and durability due to the formation of strong metallic bonds between powder particles,[9] and (iv) easy customization of the wick topology by heating and compressing copper metal powders with various powder grain sizes, sintering temperature, and pressure.[10,11] The wick structure (i.e., shape

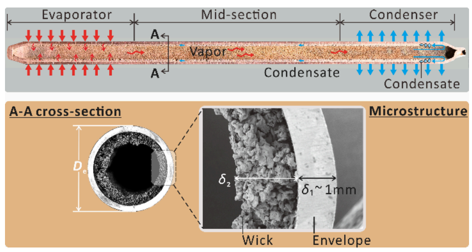

Figure 1. An original equipment manufacturer (OEM) capillary-driven heat pipe with a copper tube as envelope and sintered copper powders as wick, and microstructures (D_e = 10 mm, L = 20 mm, $\delta_1 \approx$ 1.0 mm, and $\delta_2 \approx$ 1.8 mm).

Received: January 24, 2024
Revised: March 27, 2024
Accepted: March 27, 2024
Published: April 8, 2024

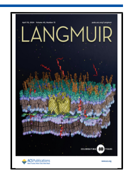

https://doi.org/10.1021/acs.langmuir.4c00307
Langmuir 2024, 40, 8194−8204

and thickness) can, therefore, be controlled, using different forms and sizes, to fit the spatial requirements of various heat pipe applications.[7,12]

For commercially available capillary-driven heat pipes with sintered copper powder wicks (Table S1), the total length (L) ranges from 20 to 305 mm while the exterior diameter (D_e) varies from 3.0 mm up to 12.7 mm. Furthermore, their total weight spans from 4 to 120 g. The envelope functions as a pressure chamber where the internal pressure of the heat pipe is set to be a near vacuum. Therefore, a minimum thickness of a given envelope (δ_1) is required to sustain a negative pressure differential between the inside and outside of the envelope. The internal pressure is determined by the operating temperature of the evaporator to which a heat source is externally attached. The external pressure is largely ambient pressure. Geometric, capillaric, and fluidic parameters of typical sintered copper powder wicks for heat pipes are collated in Table S2.

Miniaturized electronics such as (smartphones and tablets) require compact devices for thermal management; consequently, a "ultrathin heat pipe (UTHP)" that has a thickness of ≤2.0 mm provides thermal dissipation for space-limited electronics.[13−15] UTHP's are usually flattened circular section sintered copper powder heat pipes or thin wick sheet sandwiched between two metallic sheets.

In addition, biporous wick topologies have been employed to further enhance the heat spreading of heat pipes that are characterized by two distinctive lengths, whereby the smaller length scale provides sufficient capillary force and the larger reduces liquid hydraulic resistance.[5,6,16] Highly porous metallic foams consisting of stochastic open pores are an example of biporous media. The metallic foam pores can be as small as 40 μm, which enhances capillary forces while the high porosity corresponds to high permeability, and hence increase capillary pumping.[17,18] Zhou et al.[18] observed that a copper metallic foam with smaller pore wick structures provide a much larger capillary force to drive the cycle of the working fluid. Therefore, the copper foam, as a wick structure, achieved enhanced thermal performance by decreasing the thermal resistance.

For portable and aerospace applications, lightweighting is one of the important design constraints.[19,20] For this purpose, simultaneously thinning the envelope wall thickness (δ_1 in Figure 1) and making the wick structure highly porous (δ_2 in Figure 1) are approaches that can be used. Since the heat pipe is reliant on capillarity, alternative lightweight wick structures (i) need to ensure adequate capillary pumping in the wick and (ii) provide mechanical strength and stiffness to withstand external pressure applied to the envelope. In this article, we advance a capillary-driven heat pipe design by demonstrating the function of an ultrathin envelope with an integrally manufactured high porosity wick structure, to achieve lightweighting and improved thermal transport capacity.

■ DESIGN AND FABRICATION OF ULTRALIGHTWEIGHT CAPILLARY-DRIVEN HEAT PIPES

Prior to designing a lightweight envelope, two distinct failure mechanisms of the envelope need to be understood: (i) buckling during idling (i.e., without any thermal loads) and (ii) yielding during heat piping. During idling, the external surfaces of the envelope are under uniform ambient static pressure, while the internal pressure is nearly a vacuum. Thus, the compressive load causes the envelope to buckle.[21] On the other hand, during heat piping, vaporization of a working fluid at the evaporator increases the internal pressure, exceeding the external (ambient) pressure and thus yielding or rupture of the envelope is possible.[22] In the design of the ultralightweight capillary-driven heat pipe, the envelope thickness was based on the classical buckling mode theories (Section S1 in the Supporting Information), to give a conservative estimate. Here, two prototypes, e.g., D_e = 5.07 mm and 6.08 mm, were fabricated, and the thickness (δ_1) for electroless plating was selected to be $\delta_1 \approx 35$ μm and 40 μm respectively, as summarized in Table 1. The integrally plated wicking media and envelope provided additional mechanical strength to support the envelope wall from buckling.

We have sequentially formed the envelope and wick structure via electroless plating, following three broad steps: (i) preparing for a polymer (PMMA) interior template, electroless plating to form the envelope, etching out the interior template, and electroless plating of the porous wick layer onto internal envelope surfaces (Figure 2a), (ii) blackening for hydrophilicity (Figure 2b), and (iii) charging a working fluid (DI water) followed by evacuation and sealing (Figure 2c).

The fabrication of a copper envelope via electroless plating involves the deposition of a metallic impermeable layer conformally on a cylindrical polymer template, as shown by Figure 2a. Since the conventional electroless copper plating was developed for a printed circuit board for electronic circuits, etching-out the polymer substrate has rarely been considered. A poly(methyl methacrylate) (PMMA) template synthesized by a cold mounting resin is known to be compatible with copper and easily etched out by dipping in acetone.[23] Furthermore, PMMA is relatively resistant to temperature changes, compared to other polymers, and exhibits only slight shrinkage and change in shape during curing; thus, it was adopted in this study due to its inherent dimensional stability.

Two PMMA rods with differing diameters of D_{PMMA} = 5.0 and 6.0 mm were prepared. Copper electroless plating on these PMMA templates was carried out under two separate conditions: (i) first plating, which involved low-speed plating at low temperature (40 °C), and (ii) second plating, which involved high-speed plating at high temperature (70 °C). The first plating is to ensure the deposition of a copper layer at the rate of 1.0 μm/h with a pH of 13.8 for the coating solution, $Cu^{2+} + 2HCHO + 4OH^-$ while the second plating is to accelerate the deposition at 5.0 μm/h by the coating solution with a pH of 12.3. After the first plating, the template was etched out, resulting in a thin copper tube. Subsequently, the second plating deposits faster growing copper layers on both the inner and outer surfaces of the copper tube (Figure 2a). The desired thickness of the electroless plated layers to form an envelope is achieved as estimated by eq (S1) in the Supporting Information.

In a capillary-driven heat pipe, the capillarity of a given wick structure drives the condensate back to the evaporator. Hence, the wick must provide sufficient pumping via capillary force through the porous structure.[19] First, on the inner surface of the envelope fabricated via electroless plating, another stage of electroless plating is implemented to generate a porous layer as a wick structure. The basic process is the same as that for the first plating. The only difference is to add a surfactant to the plating solution to generate hydrogen (H_2) bubbles and to simultaneously keep them within the plated layer being deposited. These bubbles eventually disappear, leaving the voids in the deposited layer, which finally forms an open-cell porous layer.

The porous copper layer created by electroless plating is hydrophobic to deionized (DI) water.[24] Therefore, it is

https://doi.org/10.1021/acs.langmuir.4c00307
Langmuir 2024, 40, 8194−8204

Table 1. Parameters of the Ultralightweight Capillary-Driven Heat Pipes (uHPs) with Envelopes and Wicks Fabricated via Electroless Plating[a]

Nomenclature	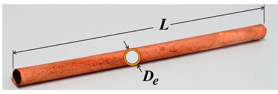		
		uHP Design 1	uHP Design 2
Envelope	Exterior diameter, D_e (mm)	5.07	6.08
	Length, L (mm)	100	100
	Thickness, δ_1 (μm)	~ 35	~ 40
	Weight (g)	0.496$^+$	0.680$^+$
Wick	Thickness, δ_2 (μm)	~ 100	~ 100
	Porosity, ε	~ 0.785	~ 0.785
	Weight (g)	0.296*	0.357*
Average weight of envelope + wick (g)		0.792 (0.95 measured)	1.037 (1.6 measured)
DI water	Weight (g)	0.5 (measured)	0.7 (measured)
Average total weight (envelope + wick + water) (g)		1.292 (1.45 measured)	1.737 (2.3 measured)
Filling ratio		~25.9%	~25.1%
(Measured data)			

D_e (mm)	Specimen	L (mm)	V_e (m^3)×10^{-6}	W_{e+w} (kg) (envelope + wick)	ρ, (W_{e+w})/V_e (kg/m^3)	ρ_e, ($W_{e+w+water}$)/V_e (kg/m^3)
	#1			0.0009	458.5	
	#2			0.0010	509.3	
5.07	#3	10	1.963	0.00075	382.1	
	#4			0.00088	448.3	
	#5			0.00122	621.5	
	Average			0.00095	483.96	738.7
D_e (mm)	Specimen	L (mm)	V_e (m^3)×10^{-6}	W_{e+w} (kg) (envelope + wick)	ρ (W_{e+w})/V_e (kg/m^3)	ρ_e ($W_{e+w+water}$)/V_e (kg/m^3)
	#1			0.00181	640.3	
	#2			0.00141	498.8	
	#3			0.00172	608.4	
	#4			0.00164	580.1	
	#5			0.00164	580.1	
	#6			0.00176	622.7	
6.08	#7	10	2.827	0.00128	452.8	
	#8			0.00125	442.2	
	#9			0.00148	523.5	
	#10			0.00167	590.7	
	#11			0.00175	619.0	
	#12			0.00182	643.8	
	#13			0.00187	661.5	
	#14			0.00162	573.0	
	#15			0.00177	626.1	
	Average			0.00160	565.97	813.6

[a]The superscripted plus sign (+) indicates data estimated from the dimensions and the density of dense copper; the asterisk symbol (*) indicates data estimated based on the porous wick having a porosity of 0.785.

necessary to impart hydrophilicity through chemical treatment. To this end, blackening was performed using a mixed solution of potassium persulfate and sodium hydroxide. The electroless-plated envelope is dipped in the aqueous solution of NaOH and $K_2S_2O_8$ at mixture of 7.5 g/L and 1.5 g/L, respectively for 3 h.[23] The blackening finally produces CuO that makes the surface hydrophilic, on the surfaces via the following sequential processes:[25] (i) $Cu + 2NaOH + K_2S_2O_8 \rightarrow Cu(OH)_2 + Na_2SO_4 + K_2SO_4$, (ii) $Cu(OH)_2 + 2OH^- \rightarrow Cu(OH)_4^{2-}$, and (iii) $Cu(OH)_4^{2-} \rightarrow CuO + 2OH^- + H_2O$. In contrast to the wick layer formed in air at a high temperature, the CuO layer after blackening forms a unique nanostructure, such as downy hair, which is a hierarchical fractal structure.[26] According to Onda et al.,[24] such a fractal surface greatly enhances hydrophilicity.

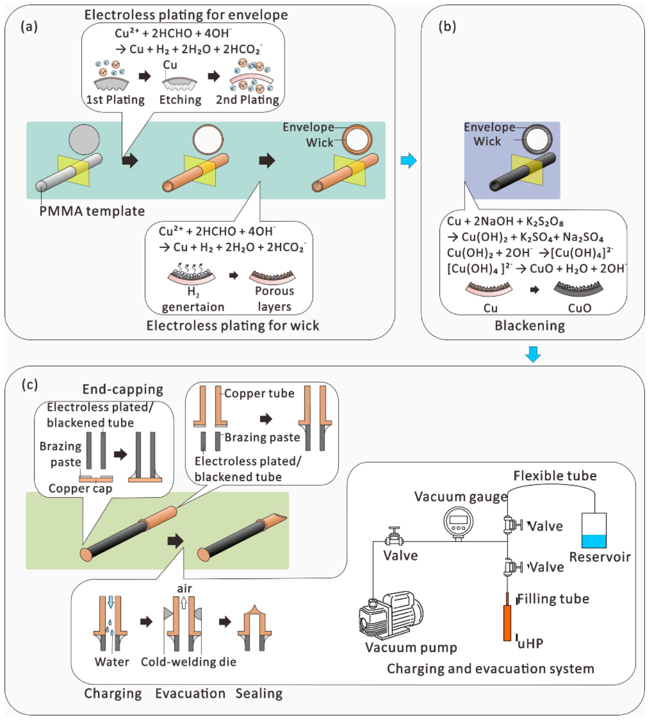

Figure 2. Fabrication process of an ultralightweight capillary-driven heat pipe: (a) envelope and wick structure via electroless plating, (b) blackening, and (c) end-capping, charging, evacuation, and sealing.

Vacuuming the envelope, termed "evacuation" after charging DI water, and sealing to complete the functioning heat pipe are illustrated in Figure 2c. First, the envelope was connected to a vacuum system via a filling copper tube. A two-stage oil sealed rotary vane vacuum pump was used for evacuation. A digital vacuum gauge monitored pressure inside the envelope during evacuation. A reservoir of DI water was connected to the system with another flexible tube. In addition, to control the amount of DI water injected into the envelope, three bellow-sealed valves were used to switch the mode between evacuation and charging. The reservoir was heated and subsequently frozen by liquid nitrogen to prevent or minimize a noncondensable gas (NCG) from being dissolved back in DI water. This process was repeated at least twice to minimize the NCG. Subsequently, the precleaned heat pipe envelope was connected to the system and evacuated at the absolute pressure of 2.1 Pa (near vacuum state). The reservoir was then reversed by bending the flexible tube to charge DI water to the envelope, resulting from pressure difference and gravity. The filling tube was then clamped before the heat pipe was removed from the system (Figure 2c). Finally, degassing was conducted by heating up the specimen from the bottom to let any remaining NCG be gathered upward in the

https://doi.org/10.1021/acs.langmuir.4c00307
Langmuir 2024, 40, 8194−8204

lower part of the filling tube, which was subsequently sealed by a cold-welding die. The charged DI water content was measured to be ~0.5 and 0.7 g for the specimen of D_e = 5.07 mm and D_e = 6.08 mm, respectively.

EXPERIMENT AND RESULTS

Capillarity Test Setup. Capillary rise is a measure of capillary pumping for a given wick structure, an important parameter that needs to be considered during the selection process of the wick material/structure. To characterize this, we measured the capillary rise (h) of both the wick fabricated by the electroless plating and blackening, and the original equipment manufacturer (OEM) sintered Cu powder wick (as a reference).

Following a method detailed by Tang et al.,[27] we constructed a test setup as illustrated in Figure 3a, which includes a cantilever

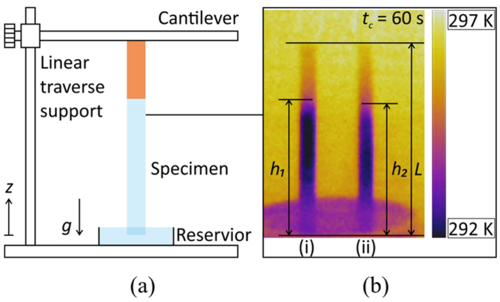

Figure 3. Capillary pumping measurement. (a) Schematic of the test setup for measuring capillary rise (h), (b) capillary rise of both (i) an electroless-plated wick (h_1) and (ii) an OEM-sintered Cu powder wick (h_2), captured by a precalibrated infrared (IR) camera where L = 90 mm.

that holds both the wick specimen and a reservoir containing DI water as the working liquid. The cantilever is vertically traversable along the z-axis, coinciding with the gravitational (g)-axis. The present wick specimen was prepared with dimensions of $H = 8.0 \times W = 8.0 \times L = 90.0$ mm. The OEM cylindrical heat pipe was cut in half by an electrical discharge machine to prepare the reference wick specimen. The height of the cantilever was set for both wicks to be submerged into the DI water, while the precalibrated infrared (IR) camera recorded temperature variation along the span of each wick specimen at the rate of 0.2 Hz (i.e., 1 frame per 5 s), as shown by Figure 3b. The absorbed DI water acts to alter the infrared emissivity difference between the wick structure and working liquid, yielding a temperature drop.[27−29] Thus, the capillary rise (h) was determined as a function of time.

Thermal Characterization Test Setup. Thermal characterization of the heat pipes was carried out using a purposely built test rig, illustrated in Figure 4. The test rig consists of a heat pipe specimen, five uniformly distributed cartridge heaters (Model CSS-10120/120, Omega, Inc.) that simulate the external heat source (Q_{in}) input at the evaporator end, a liquid-cooling unit for a condenser end, an AC power supply, an infrared (IR) camera (FLIR E8), K-type film thermocouples (Model SA1XL-K-120, Omega, Inc.), and a data acquisition unit (34872A LXI Data Acquisition/Switch Unit, Keysight). Each heat pipe was positioned vertically by a copper heating base block (with external dimensions of 30 mm (along the s-axis in Figure 4) × 20 mm × 20 mm). At the center of the heating base block, a hole of D_e, which is the exterior diameter of each uHP specimen, was drilled. An IR viewing slot and 5 holes for the

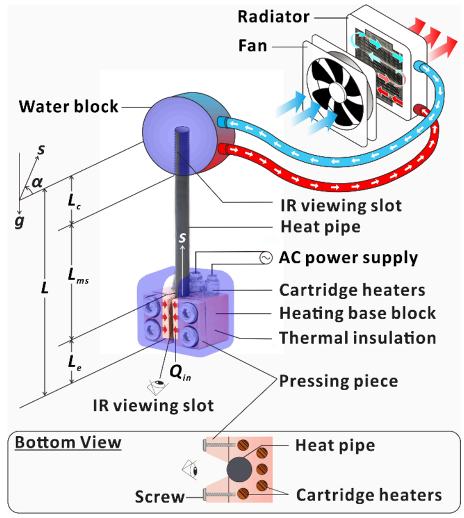

Figure 4. Schematic of the test setup for measuring thermal spreading capacity where $\alpha = 0°$ and 90° indicate that the specimen functions as a heat pipe and a thermosyphon, respectively.

cartridge heaters connected in parallel were also machined as shown in Figure 4. An input power to the cartridge heaters was regulated from 5.0 to 40.0 W, using the AC power supply. In this setup, the vapor generated in the evaporator convects upward and the condensate moves downward along the capillary passage configured along the inner envelope surfaces.

Thermal grease (with a thermal conductivity of k > 1.93 W/(m K); Model JC-500, Joycool, Inc.) was used between the heat pipe and heating base block to minimize contact thermal resistance. To further ensure a good contact, two pressing pieces with screw bolts were devised, as shown in Figure 4. The multiple layers of thermal insulation (photopolymer resin) tape (Formlabs, Inc.) covered the entire heating base block to reduce heat loss. A commercial liquid-cooling unit (Redbit 240) was used to provide thermal rejection at the condenser section to the environment under ambient conditions. The whole setup was supported by a rotation system that allows the heat piping axis (the s-axis) to be changed with respect to the gravitational g-axis, whose angle is denoted by α (measured in degrees). Here, $\alpha = 0°$ indicates that the test specimen is positioned horizontally, functioning as a heat pipe, whereas at $\alpha = 90°$, the heat pipe orientation is coincident with the gravitational axis, and the thermal spreading takes place vertically from the bottom evaporator to the top condenser, thus functioning as a thermosyphon.

Measurement Uncertainties. To evaluate heat spreading by both heat pipes, the temperature distribution along the respective heat pipes' span (i.e., the s-axis) was measured using an IR camera. Prior to measurement, the IR camera was calibrated against data obtained from film thermocouples attached on a heat pipe surface at selected locations. Temperature values from both IR camera and film thermocouples were correlated linearly (eq 1) for a wide range of heat inputs to cartridge heaters attached to heat pipe, as

$$T\ [°\mathrm{C}] = 0.99T_{\mathrm{IR}} - 0.54 \quad (1)$$

Thermal resistance (R_θ) is widely used to characterize and compare the performance of heat pipes; it is defined as

$$R_\theta = \frac{T_e - T_c}{Q_{in}} \quad (2)$$

https://doi.org/10.1021/acs.langmuir.4c00307
Langmuir 2024, 40, 8194−8204

where T_e and T_c are the average temperature of the evaporator and condenser, respectively, and Q_{in} is the total heat emitted by a heat source (or input heat). With a heater simulating such a heat source, Q_{in} is typically calculated as

$$Q_{in} = \frac{V^2}{R} \tag{3}$$

where V and R are separately the voltage supplied to heaters and electrical parallel resistance.

Measurement uncertainties were estimated using a method detailed in ref 30 as follows. If $y = f(x_1, x_2, ..., x_n)$, then the uncertainty propagated by x_i in the variable y is given by

$$\Delta y = \sqrt{\left(\frac{\partial y}{\partial x_1}\Delta x_1\right)^2 + \left(\frac{\partial y}{\partial x_2}\Delta x_2\right)^2 + ... + \left(\frac{\partial y}{\partial x_n}\Delta x_n\right)^2} \tag{4}$$

where Δx_i is the absolute uncertainty in x_i. Equation 4 was used to estimate the uncertainty of thermal resistance (R_θ) that was associated with wall temperatures measured by the IR camera at both the evaporator and condenser ends (i.e., T_e and T_c) whose accuracy and resolution are ±2.0% and 0.1 °C, respectively. The uncertainty of thermal resistance was calculated to be within ±8.6%, governed predominantly by the surface temperatures.

DISCUSSION OF RESULTS

Microstructures and Capillarity. In this study, we evaluated the structural and thermal transport performance of a novel ultralight capillary-driven heat pipe (uHP). For reference, we have compared our heat pipe to a commercially available original equipment manufacturer (OEM) heat pipe that is wicked by sintered Cu powders.

We have fabricated, in total, 20 uHPs: 5 specimens with an exterior diameter of D_e = 5.07 mm and 15 specimens with an exterior diameter of D_e = 6.08 mm, as shown in Table 1. In the following analysis, the data measured from a representative specimen of D_e = 6.08 mm are mainly presented. The uHP features an envelope and wick structure that are ultra-lightweighted by electroless plating (Figure 5). The envelope

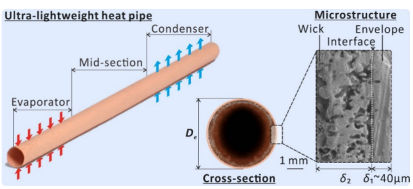

Figure 5. Configuration and microstructure of a prototype ultralight capillary-driven heat pipe (uHP) for $D_e \approx 6.08$ mm, L = 100 mm, δ_1 = 40 μm, and δ_2 = 100 μm.

has an impermeable wall with a mean thickness of 40 μm, functioning as a vacuum chamber whose absolute internal pressure is set and measured to be ∼2.1 Pa. The inner surfaces are deposited with a 100-μm-thick porous layer to facilitate capillary-driven flow of the condensate through the porous wick structure during heat piping.

The microstructure of a raw copper wick fabricated via electroless plating prior to blackening (Figure 6a) is hydrophobic.[24] For example, sequential images by a high-speed camera show that a drop of DI water falling onto the unblackened wick layer clearly exhibits hydrophobicity, since the drop free falls normal to the surface, impacts the surface, and then bounces back, but immediately returns to sit on the *unwetted* wick surface, where the contact angle is estimated to be $\theta \approx 72°$. On the other hand, after blackening (Figure 6b), the free-falling water drop is absorbed by and spread within the porous wick layer in its immediate contact due to super-hydrophilicity.

Good heat spreading that is achieved by any capillary-driven heat pipe is attributed to effective capillary pumping by a wick structure. Thus, the pumping effectiveness of the wick can be characterized by the capillary rise. Here, the capillary pumping of the electroless-plated porous wick layer was tested using a setup shown in Figure 3. Results are compared with the OEM-sintered Cu powder wick. Temperature distributions along the length of the electroless-plated wick (s/L) at selected time frames, extracted from IR images are plotted in Figure 7a. The absorbed DI water by capillary forces decreases the temperature of the wet wick section, as indicated by the lowered temperature on the IR images. We define capillary rise ($h(t)$) as the point when the wick temperature begins to drop, as indicated in Figure 7a.

The capillary rise (h) at a given moment is plotted in Figure 7b showing that the capillary rise for the two test specimens (i.e., uHP and OEM) behaves in a similar manner. Based on the measured capillary rise in time (t) recorded, its rate (i.e., $\mathrm{d}h(t)/\mathrm{d}t$) was calculated as included. There is an initial steep rise. Thereafter, an asymptotic decrease in the rate of the capillary rise follows. This common behavior is attributed to the capillary pressure ($\Delta P_c = 2\sigma \cos \theta / r$) during the capillary rise that is associated with pressure drop and friction forces, governed as

$$\frac{\mathrm{d}h(t)}{\mathrm{d}t} = \frac{\Delta P_c K}{\mu \varepsilon}\left(\frac{1}{h(t)}\right) - \frac{Kg\rho}{\mu\varepsilon} \tag{5}$$

where σ, μ, and ρ are the surface tension, viscosity, and density of the working fluid (DI water), respectively; g is the gravitational acceleration; and K, ε, θ, and r are the permeability, porosity, contact angle, and effective radius of a given porous wick, respectively.[31] Similar capillary pumping is achieved by the porous wick layer fabricated via electroless plating and an OEM-sintered Cu powder wick, in the present setup.

In eq 5, thermophysical parameters such as ρ and μ are fixed for a given working fluid i.e., DI water and the topology-dependent parameter K/ε for both wick structures are defined. Given that the prior estimation of the porosity (ε) for the uHP wick being roughly ε_{uHP} = 0.785 (Section S2 in the Supporting Information), the capillary pressure (ΔP_c) and permeability (K_{uHP}) may be separately estimated by fitting the experimental data with the exact solution[32] for eq 5,

$$h(t) = \frac{\alpha}{\beta}[1 + W(-\mathrm{e}^{-1-\beta^2 t/\alpha})] \tag{6}$$

where α and β are given as

$$\alpha = \frac{P_c K}{\mu \varepsilon} = \frac{2\sigma K \cos\theta}{\mu \varepsilon r}$$

$$\beta = \frac{Kg\rho}{\varepsilon \mu}$$

and $W(z)$ is the Lambert W function, $z = W(z)e^{W(z)}$. Here, z is a dummy variable. Results are also included in Figure 7b and are summarized in Table 2. In comparison to the tested OEM-sintered powder wick structure, the uHP wick provides 20% higher resultant capillary pressure with 25% lower permeability and 67% higher porosity. Collectively, the wick structure of the uHP functions to reach 20% higher Jurin's height, which is the

https://doi.org/10.1021/acs.langmuir.4c00307
Langmuir 2024, 40, 8194−8204

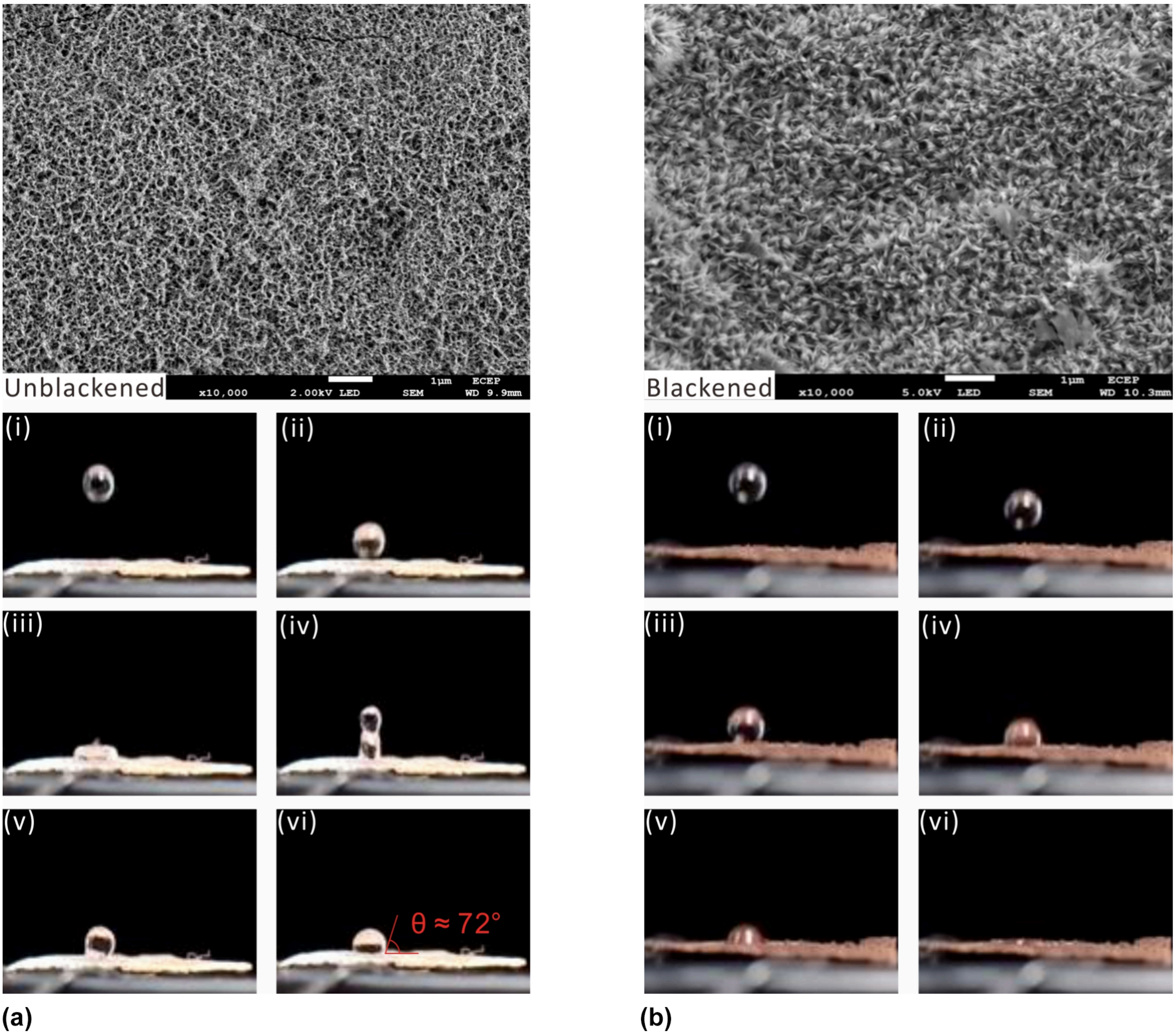

Figure 6. Wettability tests comparing the wick surface treatments: (a) unblackened, raw copper wick with hydrophobic droplet formation and a contact angle that was measured to be $\theta \approx 72°$; and (b) superhydrophilicity ($\theta \to 0°$) of a porous wick layer after blackening.

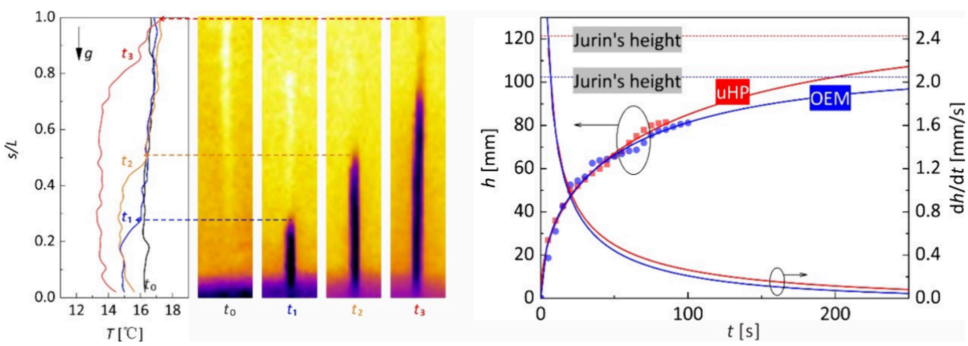

Figure 7. Capillarity, shown by (a) the determination of capillary rise from measured IR images and (b) determination of capillary rise ($h(t)$) and its rate ($dh(t)/dt$ along the blackened porous wick layer at $\alpha = 90°$ and comparison with an OEM sintered copper powder wick structure.

limit of capillary rise for a given tube diameter, and thus at least equivalent heat spreading to the OEM's sintered copper powder wick is expected.

Heat Spreading. The variation of the surface temperature along any given heat pipe is indicative of a heat spreading capability. An effective heat pipe (i) minimizes thermal resistance ($R_\theta = (T_e - T_c)/Q_{in}$)) for a minimal temperature

https://doi.org/10.1021/acs.langmuir.4c00307
Langmuir 2024, 40, 8194−8204

Table 2. Capillaric and Topological Parameters of the uHP and OEM Wick Structures, Estimated by Fitting the Measurement Data in Figure 5d By Using eq 6

	ΔP_c [Pa]	K^a [m^2]	ρ of DI water [kg/m^3]	μ of DI water [Pa s]	ε
OEM	1001.30	3.89×10^{-11}	998.2	0.001	0.470
uHP	1190.02	2.93×10^{-11}			0.785

[a] K for sintered copper powders: 4.75×10^{-12}–1.65×10^{-10} m^2.[33−36]

drop between evaporator and condenser, and (ii) reduces the operating temperature of the evaporator (T_e) for a given heat input (Q_{in}). Here, T_c is the condenser temperature. Thus, the characteristics of a uniform-like temperature distribution along the span of a heat pipe and a low evaporator temperature when heated are desired.[20]

Figure 8a displays how heat is spread through both uHP and OEM specimens from the evaporator to the condenser for four selected input heat values of Q_{in} = 10, 20, 30, and 40 W at α = 90°, functioning as a thermosyphon. Here, the OEM heat pipe is wicked by sintered Cu powders with L = 90 mm, D_e = 6.0 mm, D_i = 4.9 mm, δ_1 = 0.66 mm, and a water content of 0.53 g. In both specimens, the vapor that is generated in the evaporator flows upward, and the condensate at the condenser moves downward by gravitational acceleration. The one-to-one comparison with the prototype uHP is made by measurement of the surface temperature with respect to ambient temperature ($T - T_\infty$), varying along the span (s/L) where s/L = 0.0 and 1.0 denote the evaporator and condenser ends, respectively. For the OEM heat pipe, the surface temperature at each section (evaporator (E), midsection (M-E), and condenser (C)) is roughly constant yet drops at the intermediate sections between the evaporator and the midsection (s/L = 0.2), and the midsection and the condenser (s/L = 0.8). On the other hand, the temperature drop for the uHP is greater than the OEM heat pipe. The temperature variation in 0.2 < s/L < 0.8 is largely constant having similar values. Specifically at Q_{in} = 5.0 W, the surface temperature of the uHP decreases steeply away from the end-cap of the evaporator. Overall, both heat pipes operate at similar temperatures.

Now, both specimens are positioned horizontally (i.e., α = 0°) and function as heat pipes. Unlike the foregoing case, the condensate returns to the evaporator through the wick structure by capillary pumping, without assistance from gravitational acceleration. The one-to-one comparison of overall heat spreading is plotted in Figure 8b for the four selected heat input values. The spanwise temperature distribution is qualitatively similar to that in Figure 8a. However, Figure 8b shows that the uHP operates at substantially lower temperatures than the OEM heat pipe, e.g., ~25% lower at 30 and 40 W over its entire span during heat piping; thus, the electrical component attached to the evaporator end maintains a lower temperature.

The heat spreading of the uHP is further characterized in the heat input range of 5.0 W ≤ Q_{in} ≤ 45.0 W. To this end, the thermal resistance (R_θ) is used for a given heat input, with lower values indicating favorable spreading performance. Figure 8c compares the thermal resistance between the uHP and the OEM, with two separate datasets to demonstrate the improved thermal performance of the uHP. Here, one set was obtained using a purchased OEM heat pipe wicked by sintered Cu powders that was tested using a custom-built experimental setup. The other data were from refs 27,37−40, who tested tubular heat pipes with sintered Cu powders, having similar dimensions to the present OEM heat pipe. Comparison between

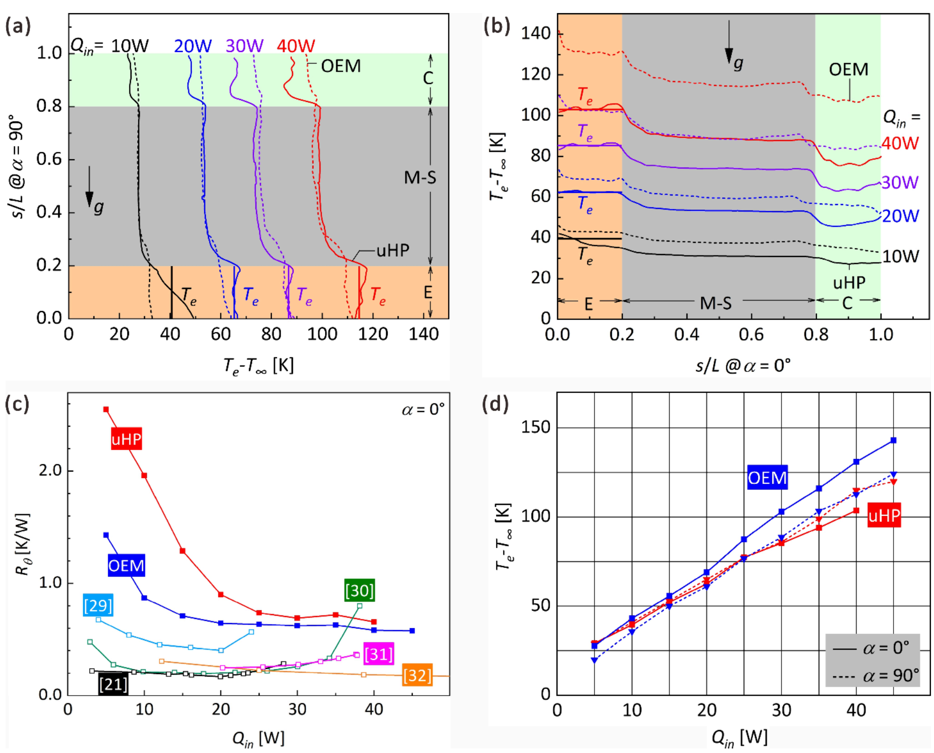

Figure 8. Thermal analysis and comparison: (a) Temperature distributions along the exterior surface of the uHP and OEM heat pipe specimens functioning as a thermosyphon (α = 90°) with a water-cooling unit attached at their tip where E, M-S, and C stand for evaporator, midsection, and condenser, respectively, (b) Temperature distributions along the exterior surface of both the uHP and OEM heat pipe specimens functioning as a heat pipe (α = 0°), (c) thermal resistance (R_θ) varying with heat input (Q_{in}), (d) evaporator temperature ($T_e - T_\infty$) varying with heat input (Q_{in}).

https://doi.org/10.1021/acs.langmuir.4c00307
Langmuir 2024, 40, 8194−8204

the two OEM heat pipes shows agreement in the considered heat input range, providing a thermal resistance (R_θ) of ~0.7 K/W, thus further demonstrating the credibility of the experimental setup.

The results of Figure 8c also show that the thermal resistance of the uHP decreases steeply from 2.5 K/W to 0.7 K/W within a heat input range from 5.0 W to 25.0 W. As the heat input is further increased up to Q_{in} = 45.0 W, the thermal resistance approaches an asymptotic value of ~0.7 K/W. Thus, the heat spreading by the uHP becomes equivalent to the OEM heat pipe in the range of heat inputs (25.0 W ≤ Q_{in} ≤ 45.0 W). The equivalent heat spreading by the uHP resulted from the effective condensate pumping caused by the blackened porous wick that is fabricated via electroless plating.

As a result of heat spreading along a heat pipe and heat rejection at the condenser end, the operating temperature of a given heat source (e.g., electronic chip) or the evaporator temperature of a given heat pipe is reduced. Therefore, the operating temperature of the evaporator may be another measure of the thermal characteristics of a given cooling unit, typically consisting of, e.g., a heat pipe, a liquid circulation pump, fins, and a fan. Under identical cooling and operating conditions, the evaporator temperature of both heat pipes in ($T_e - T_\infty$) is compared in Figure 8d at 5.0 W ≤ Q_{in} ≤ 45.0. For both specimens, the evaporator temperature increases monotonically as the input heat increases. The uHP provides similar temperatures to the OEM heat pipe at the low heat input range (5.0 W ≤ Q_{in} ≤ 25.0), and no apparent degradation of the cooling performance of the uHP is observed due to the orientation (i.e., functioning either as a thermosyphon ($\alpha = 90°$) or a heat pipe ($\alpha = 0°$)). The OEM heat pipe exhibited an ~25% increase in the evaporator temperature when working as the horizontal heat pipe, compared to that of a thermosyphon in the entire range of the heat input considered. In comparison, at Q_{in} > 25 W, the evaporator temperature ($T_e - T_\infty$) of the uHP is ~25% lower than that of the OEM heat pipe, thus demonstrating that the uHP has enhanced thermal rejection that facilitated lower evaporator operating temperatures.

Thermal Analysis. A question naturally arises as to why the uHP's evaporator operates at a 25% lower temperature than the OEM at Q_{in} > 25 W, despite a slightly higher thermal resistance (R_θ is ~12.7% higher) in Figure 8c and similar charged DI water mass (~0.5 g). To squarely address this question, an energy balance analysis was performed to understand the relationship that which exists between the operating temperature of the evaporator (T_e) and heat loss (Q_{loss}) where the input heating power (Q_{in}) for the uHP and OEM are equivalent.

We consider a generic capillary-driven heat pipe (illustrated in Figure 9), which has a heating power input (Q_{in}) at the evaporator end, with an average temperature T_e). In the midsection, there is heat loss (Q_{loss}) through the envelope wall to the surroundings under ambient conditions (heat transfer occurs through the heat pipe wall to the surroundings). The condenser end has an average temperature (T_c) where heat is removed (Q_{out}) via convective cooling, and U is the overall convective heat transfer (W/(m^{2}K)) and A is the heat-transfer area (m^2). The objective is to demonstrate with energy balance considerations how the operating temperature of the evaporator (T_e) is related to the heat loss (Q_{loss}) through the midsection wall. Note that, in the conventional thermodynamic analysis for capillary-driven heat pipes, the heat loss is typically assumed to be negligible as being adiabatic (i.e., $Q_{loss} = 0$).

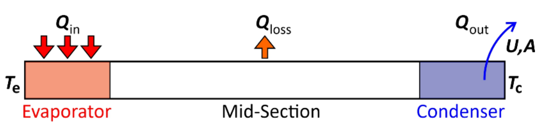

Figure 9. Schematic of a heat pipe that shows the evaporator operating temperature and the respective heat flows *into* and *out of* the heat pipe.

Using the conservation of energy, the input power (Q_{in}) is equal to the sum of heat loss (Q_{loss}) and heat rejected (Q_{out}) from the condenser end as

$$Q_{in} = Q_{out} + Q_{loss} \tag{7}$$

The input heating power (Q_{in}) is also related to the overall thermal resistance (R_θ) across the evaporator and the condenser, by definition, as

$$R_\theta = \frac{T_e - T_c}{Q_{in}} \Rightarrow Q_{in} = \frac{(T_e - T_c)}{R_\theta} \tag{8}$$

The heat rejected at the condenser end is determined by heat transfer to the surroundings at ambient temperature (T_∞), where U is the overall heat-transfer coefficient and A is the heat-transfer area. expressed as

$$Q_{out} = UA(T_c - T_\infty) \tag{9}$$

Substitution of eqs 8 and 9 into eq 7 yields

$$\frac{(T_e - T_c)}{R_\theta} = UA(T_c - T_\infty) + Q_{loss} \tag{10}$$

Further simplifying and rearranging eq 10 for the evaporator temperature (T_e) leads to

$$T_e = (1 + R_\theta UA)T_c - R_\theta UAT_\infty + R_\theta Q_{loss} \tag{11}$$

From eq 8, the condenser temperature (T_c) is found to be

$$R_\theta = \frac{T_e - T_c}{Q_{in}} \Rightarrow T_c = T_e - R_\theta Q_{in} \tag{12}$$

Substitution of eq 12 into eq 11 gives

$$T_e = (1 + R_\theta UA)(T_e - R_\theta Q_{in}) - R_\theta UAT_\infty + R_\theta Q_{loss} \tag{13}$$

Equation 13 can be reduced to,

$$T_e = \frac{Q_{in}}{UA} + R_\theta Q_{in} + T_\infty - \frac{Q_{loss}}{UA} \tag{14}$$

The final expression (eq 14) explicitly indicates that, for given heat input through the evaporator end (Q_{in}) and heat rejection at the condenser end (UA) of a heat pipe, both thermal resistance along the heat pipe span (R_θ) and heat loss through the midsection surface (Q_{loss}) determine the evaporator's operating temperature, T_e. Specifically, lowered R_θ acts to decrease T_e, whereas the increased Q_{loss} results in a decrease in T_e.

On the other hand, the uHP has a slightly higher thermal resistance than the OEM, which may cause an adverse effect, acting to increase T_e. However, despite the marginally higher thermal resistance, our energy balance-based analysis (eq 14) implies that higher heat loss through the uHP's ultrathin envelope wall may cause the reduced evaporator operating temperature, among other possible contributing factors, which could not be stipulated at present. Specifically, the heat loss across the envelope wall is a consequence of the condensate

https://doi.org/10.1021/acs.langmuir.4c00307
Langmuir 2024, 40, 8194−8204

temperature in the midsection being above the surrounding temperature (T_∞), which allows heat transfer *from* the heat pipe *to* the surroundings to take place. The uHP can further enhance the heat transfer compared to the OEM heat pipe due to the ultralightweighted construction. The electroless plating creates an integrally connected wick ($\delta_2 \approx 100\ \mu$m) and ultrathin envelope ($\delta_2 \approx 40\ \mu$m) that minimizes contact resistance between the wick ligaments and the inner surface of the envelope. In addition, the high porosity open cellular wick improves condensate mixing and increases the internal heat transfer surface area to enhance heat transfer from the condensate. Furthermore, based on the similar permeability for both heat pipes estimated (Table 2), pressure drop across both wick structures could be assumed to be similar. For the same amount of condensate flowing through each wick structure, the Reynolds number of condensate in the uHP could be estimated to be substantially higher (i.e., ~20 times thinner wick yet ~2 times higher porosity, leading to ~10 times smaller condensate flow area in the uHP wick). Thus, collectively, the uHP via the ultrathin envelope wall can further enhance the heat loss (Q_{loss}), compared to the OEM heat pipe, yielding the observed ~25% lower evaporator temperature, despite the observed slightly higher thermal resistance.

Lightweighting. Demands for advanced heat pipes may be classified into three categories: (a) maximizing heat spreading, consequently reducing the operating temperature of attached electronic components; (b) compacting (reducing volume); and (c) lightweighting. For mobile applications, both compacting and lightweighting are desired with a possible improvement in heat spreading.[20]

The total weight of a given capillary-driven heat pipe is constituted by the weight of three components (envelope, wick structure, and working fluid). For both uHP and OEM heat pipes having similar exterior dimensions with a similar amount of the charged DI water (~0.5 g), ultralightweighting the heat pipe is achieved by the ultrathin-walled envelope and wick. Figure 10 depicts that the effective density (ρ_e) of OEM heat

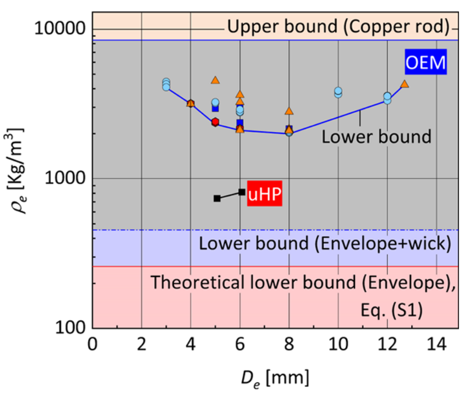

Figure 10. Effective density (ρ_e) as a measure of lightweighting, varying with the exterior diameter of capillary-driven heat pipes (D_e) and comparison with OEM heat pipes (Table S1).

pipes is decreased from ~4500 kg/m^3 as their exterior diameter is increased from D_e = 3.0 mm to D_e = 8.0 mm (ρ_e ~ 2100 kg/m^3). After the density minima when the diameter is D_e = 8.0 mm, the density variation increases for larger diameters. Specifically, for D_e = 5.0 mm and 6.0 mm, the effective density of OEM heat pipes is ~3450 kg/m^3 and 2550 kg/m^3 as a respective average value with the range of 2400 kg/m^3 ≤ ρ_e ≤ 4500 kg/m^3 and 2100 kg/m^3 ≤ ρ_e ≤ 3000 kg/m^3 in Table S1. In comparison, the two prototype ultralight heat pipes (uHPs) with D_e = 5.07 and 6.08 mm provide approximately 78% (738.7 kg/m^3 for the uHP with D_e = 5.07 mm) and 68% (813.6 kg/m^3 for the uHP with D_e = 6.08 mm) demonstrate a *reduced* effective density, with respect to each average value. This substantial lightweighting is made possible by electroless plating the envelope and wick structure.

■ CONCLUSIONS

We proposed an advanced capillary-driven heat pipe that was ultralightweighted, in comparison to its most popular commercial counterparts. This account details the process of design, fabrication, and characterization. For ultralightweighting, both envelope and wick structure were electroless plated. In particular, the wick structure composed of a microporous layer was superhydrophilized by blackening for improved capillary pumping. A series of capillary and thermal characterizations have demonstrated our groundbreaking lightweighting of a capillary-driven heat pipe that weighs, on average, only 27% of commercial counterparts wicked by sintered copper powders in similar external dimensions. Furthermore, the present ultralightweight capillary-driven heat pipe operates at 25% lowered evaporator temperature with a slightly worse heat spreading than the commercial counterparts.

■ ASSOCIATED CONTENT

Supporting Information

The Supporting Information is available free of charge at https://pubs.acs.org/doi/10.1021/acs.langmuir.4c00307.

Estimation of the envelope thickness as a long cylindrical vacuum chamber; porosity of a porous copper wick structure deposited on the envelope surface (PDF)

■ AUTHOR INFORMATION

Corresponding Author

Kiju Kang — *School of Mechanical Engineering, Chonnam National University, Gwangju 61186, South Korea;* orcid.org/0000-0002-0759-7490; Email: kjkang@chonnam.ac.kr

Authors

Yong Ju Lee — *School of Mechanical Engineering, Chonnam National University, Gwangju 61186, South Korea*

Yi Xiang Wang — *School of Mechanical Engineering, Chonnam National University, Gwangju 61186, South Korea;* orcid.org/0000-0002-1736-4746

Yoon Chang Jeong — *School of Mechanical Engineering, Chonnam National University, Gwangju 61186, South Korea*

Michael D. Atkins — *School of Mechanical, Industrial and Aeronautical Engineering, University of the Witwatersrand, Johannesburg 2000, South Africa;* orcid.org/0000-0002-9903-9719

Tongbeum Kim — *MIIT Key Laboratory of Multifunctional Lightweight Materials and Structures, Nanjing University of Aeronautics and Astronautics, Nanjing 210016, China*

Complete contact information is available at: https://pubs.acs.org/10.1021/acs.langmuir.4c00307

Notes

The authors declare no competing financial interest.

Biographies

Yoon Chang Jeong is a Post-Doctorate Research Fellow at Materials Strength Laboratory, School of Mechanical Engineering, Chonnam National University (CNU), South Korea. He received his M.Sc. and Ph.D. at the same university in 2018 and 2023, respectively. His research interests include microarchitectured pressure vessels and mechanical metamaterials.

Michael D. Atkins is a Senior Lecturer at the School of Mechanical, Industrial and Aeronautical Engineering, University of the Witwatersrand, Johannesburg, South Africa. He received a B.Eng. (First Class Honors) from the University of the West of England, Bristol, U.K. and an M.Sc. (with Distinction) and a Ph.D. in Thermo/fluids from the University of the Witwatersrand, South Africa, and is specialized in fundamental and applied aerodynamics, active flow control, thermo-fluids in gas turbine engines, particle image velocimetry (PIV), and planar laser visualization.

Kiju Kang is a Professor at Chonnam National University, South Korea. He received a Ph.D. and M.Sc. in Mechanical Engineering from the Korea Advanced Institute of Science and Technology, South Korea. His current research interests are in mechanical metamaterials, wire-woven materials, pressure vessels, and microarchitectural shell structures (Shellulars).

Tongbeum Kim is a Distinguished Professor at the College of Aerospace Engineering, Nanjing University of Aeronautics and Astronautics, China. He obtained a Ph.D. from the University of Cambridge, U.K. after an M.Sc. from the Georgia Institute of Technology, USA and a B.Eng. from Kyung Hee University, South Korea. His current research interests are in gas turbine blade cooling, single-winged drones, and multifunctional cooling systems for drones and portable electronics.

■ ACKNOWLEDGMENTS

This work was financially supported by the Ministry of Science and ICT of Korea via the National Research Foundation of Korea (Grant No. 2021R1A2C3007705).

■ REFERENCES

(1) Faghri, A. Review and Advances in Heat Pipe Science and Technology. *J. Heat Transfer* **2012**, *134* (12), 123001.
(2) Faghri, A. Heat Pipes: Review, Opportunities and Challenges. *Front. Heat Pipes* **2014**, *5* (1), 1−48.
(3) Celsia. Types of heat pipes. Available via the Internet at: https://celsiainc.com/heat-sink-blog/types-of-heat-pipes/.
(4) Morooka, S.; Kuroki, T.; Waki, T. Study on the Heat Pipe 3rd Report, Heat Transfer Mechanism in the Evaporator of Heat Pipe with Screen Mesh Wick. *Bull. JSME* **1981**, *24* (196), 1811−1819.
(5) Semenic, T.; Catton, I. Experimental Study of Biporous Wicks for High Heat Flux Applications. *Int. J. Heat Mass Transfer* **2009**, *52* (21−22), 5113−5121.
(6) Chan, C. W.; Siqueiros, E.; Ling-Chin, J.; Royapoor, M.; Roskilly, A. P. Heat Utilisation Technologies: A Critical Review of Heat Pipes. *Renew. Sust. Energy Rev.* **2015**, *50*, 615−627.
(7) Vasiliev, L. L.; Kulakov, A. G.; Filatova, O. S.; Epifanov, S. V. Copper Sintered Powder Wick Structures of Miniature Heat Pipes. In *Proceedings of the VI Minsk International Seminar "Heat Pipes, Heat Pumps, Refrigerators"*, Minsk, Belarus, Sept. 12−15, 2005; Vol. *1*, pp 149−156.
(8) Popova, N.; Schaeifer, C.; Avenas, Y.; Kapelski, G. Fabrication and Experimental Investigation of Innovative Sintered Very Thin Copper Heat Pipes for Electronics Applications. In *37th IEEE Power Electronics Specialists Conference*, Jeju, South Korea, 2006; pp 1−5.
(9) Mahaidin, A. A.; Abdullah, N.; Mohammad, M.; Omar, M. A.; Suleiman, M. J.; Zainon, N. M.; Hadi, M. A. N.; Abd Jalil, M. N.; Omar, A. Z.; Mohd Hijazi, M. B. Effect of Sintering Cycle on Physical and Mechanical Properties of Open Pore Cell Copper Foam. *Procedia Chem.* **2016**, *19*, 546−551.
(10) Nemec, P. Porous Structures in Heat Pipes. In *Porosity—Process, Technologies and Applications*, Ghrib, T., Ed.; InTech: London, 2018; pp 141−179.
(11) Leong, K. C.; Liu, C. Y.; Lu, G. Q. Characterization of Sintered Copper Wicks Used in Heat Pipes. *J. Porous Mater.* **1997**, *4* (4), 303−308.
(12) Seong, Y.; Kim, Y.; German, R.; Kim, S.; Kim, S. G.; Kim, S. J.; Kim, H. J.; Park, S. J. Dominant Mechanisms of the Sintering of Copper Nano-Powders Depending on the Crystal Misalignment. *Comput. Mater. Sci.* **2016**, *123*, 164−175.
(13) Tang, H.; Tang, Y.; Wan, Z.; Li, J.; Yuan, W.; Lu, L.; Li, Y.; Tang, K. Review of Applications and Developments of Ultra-Thin Micro Heat Pipes for Electronic Cooling. *Appl. Energy* **2018**, *223*, 383−400.
(14) Cui, Z.; Jia, L.; Wang, Z.; Dang, C.; Yin, L. Thermal Performance of an Ultra-Thin Flat Heat Pipe with Striped Super-Hydrophilic Wick Structure. *Appl. Therm. Eng.* **2022**, *208*, 118249.
(15) Li, J.; Lv, L. Experimental Studies on A Novel Thin Flat Heat Pipe Heat Spreader. *Appl. Therm. Eng.* **2016**, *93*, 139−146.
(16) Chen, B. B.; Liu, W.; Liu, Z. C.; Li, H.; Yang, J. G. Experimental Investigation of Loop Heat Pipe with Flat Evaporator Using Biporous Wick. *Appl. Therm. Eng.* **2012**, *42*, 34−40.
(17) Han, X. H.; Wang, Q.; Park, Y. G.; T'Joen, C.; Sommers, A.; Jacobi, A. A Review of Metal Foam and Metal Matrix Composites for Heat Exchangers and Heat Sinks. *Heat Transfer Eng.* **2012**, *33* (12), 991−1009.
(18) Zhou, W.; Ling, W.; Duan, L.; Hui, K. S.; Hui, K. N. Development and Tests of Loop Heat Pipe with Multi-Layer Metal Foams as Wick Structure. *Appl. Therm. Eng.* **2016**, *94*, 324−330.
(19) Richter, R.; Gottschlich, J. M. Thermodynamic Aspects of Heat Pipe Operation. *J. Thermophys. Heat Transfer* **1994**, *8* (2), 334−340.
(20) Brennan, P. J.; Kroliczek, E. J. *Heat Pipe Design Handbook*, Vol. *1*; NASA, 1979, Contract No. NAS5423406.
(21) Timoshenko, S. P.; Gere, J. M. *Theory of Elastic Stability*; McGraw−Hill: New York, 1961; pp 289.
(22) Lardner, T. J.; Archer, R. R. *Mechanics of Solids: An Introduction*; McGraw−Hill: New York, 1994; pp 528.
(23) Min, J.; Wu, X.; Gao, F. Hydrophilic Treatments of Copper Finned Tube Evaporators. In *International Refrigeration and Air Conditioning Conference*, West Lafayette, IN, USA, 2008.
(24) Onda, T.; Shibuichi, S.; Satoh, N.; Tsujii, K. Super-Water-Repellent Fractal Surfaces. *Langmuir* **1996**, *12* (9), 2125−2127.
(25) Qiu, M.; Wang, N.; Cui, Z.; Liu, J.; Hou, L.; Liu, J.; Hu, R.; Zhang, H.; Zhao, Y. Evolution of Copper Oxide Nanoneedle Mesh with Subtle Regulated Lyophobicity for High Efficiency Liquid Separation. *J. Mater. Chem. A* **2018**, *6*, 817−822.
(26) Periyayya, U.; Madhu, D.; Subramaniyam, K.; Son, H.; Lee, I. Enhanced Cyclic Performance Initiated via an in Situ Transformation of Cu/CuO Nanodisk to Cu/CuO/Cu_2O Nanosponge. *Environ. Sci. Pollut. Res.* **2021**, *28*, 6459−6469.
(27) Tang, H.; Lian, L.; Zhang, J.; Liu, Y. Heat Transfer Performance of Cylindrical Heat Pipes with Axially Graded Wick at Anti-gravity Orientations. *Appl. Therm. Eng.* **2019**, *163*, 114413.
(28) Tang, Y.; Deng, D.; Lu, L.; Pan, M.; Wang, Q. Experimental investigation on capillary force of composite wick structure. *Exp. Therm. Fluid. Sci.* **2010**, *34*, 190−196.
(29) Yang, H.; Yang, Y.; Ma, B.; Zhu, Y. Experimental study on capillary microflows in high porosity open-cell metal foams. *Micromachines* **2022**, *13* (12), 2052.
(30) Coleman, H. W.; Steele, W. G. *Experimentation, Validation, and Uncertainty Analysis for Engineers*, Third Edition; Wiley: New York, 2018.
(31) Li, H.; Fang, X.; Li, G.; Zhou, G.; Tang, Y. Investigation on Fabrication and Capillary Performance of Multi-scale Composite Porous Wick Made by Alloying-Dealloying Method. *Int. J. Heat Mass Transfer* **2018**, *127*, 145−153.
(32) Fries, N.; Dreyer, M. An Analytic Solution of Capillary Rise Restrained by Gravity. *J. Colloid Interface Sci.* **2008**, *320* (1), 259−263.

(33) Pruzan, D. A.; Klingensmith, L. K.; Torrance, K. E.; Avedisian, C. T. Design of High-Performance Sintered-Wick Heat Pipes. *Int. J. Heat Mass Transfer* **1991**, *34* (6), 1417−1427.
(34) Leong, K. C.; Liu, C. Y.; Lu, G. Q. Characterization of Sintered Copper Wicks Used in Heat Pipes. *J. Porous Mater.* **1997**, *4* (4), 303−308.
(35) Deng, D.; Liang, D.; Tang, Y.; Peng, J.; Han, X.; Pan, M. Evaluation of Capillary Performance of Sintered Porous Wicks for Loop Heat Pipe. *Exp. Therm. Fluid Sci.* **2013**, *50*, 1−9.
(36) Sebayang, A. M. S.; Tetuko, A. P.; Nurdiyansah, L. F.; Asri, N. S.; Setiadi, E. A.; Sebayang, P. Wick Parameters (Particle Size, Porosity and Contact Angle) and Performances of a U-Shaped Heat Pipe: Experimental, Analytical and Numerical. *Aust. J. Mech. Eng.* **2022**, *0*, 1−14.
(37) Maziuk, V.; Kulakov, A.; Rabetsky, M.; Vasiliev, L.; Vukovic, M. Miniature Heat-Pipe Thermal Performance Prediction Tool − Software Development. *Appl. Therm. Eng.* **2001**, *21* (5), 559−571.
(38) Park, K.; Lee, W.; Lee, K.; Baek, I.; Rhi, S.; Shin, D. Study on the Operating Characteristics in Small Size Heat Pipe Using Nanofluids. In *Proceedings of the 3rd IASME/WSEAS International Conference on Heat Transfer, Thermal Engineering and Environment*, Corfu, Greece, 2005; pp 106−109.
(39) Wong, S.; Hsu, Z.; Hsu, L. On the Test Setting at Condenser in Thermal Performance Tests of Heat Pipes. In *Proceedings of the ASME 2017 Fluids Engineering Division Summer Meeting*, Waikoloa, HI, USA, 2017; Paper No. V01BT06A018.
(40) Mahdavi, M.; Tiari, S.; De Schampheleire, S.; Qiu, S. Experimental Study of the Thermal Characteristics of a Heat Pipe. *Exp. Therm. Fluid Sci.* **2018**, *93*, 292−304.